Simultaneous regulation of thermodynamic and kinetic behavior on FeN$_3$P$_1$ single-atom configuration by Fe$_2$P for efficient bifunctional ORR/OER

Enze Zhu [a,b], Chaoyang Shi [a,b], Jie Yu [c], Haodong Jin [a,b], Linxiang Zhou [a,b], Xikun Yang [d], Mingli Xu [a,b,*]

[a] *Faculty of Metallurgical and Energy Engineering, Kunming University of Science and Technology, Kunming 650093, China*
[b] *National and Local Joint Engineering Research Center of Lithium-ion Batteries and Materials Preparation Technology, Kunming 650093, China*
[c] *Faculty of Materials Science and Engineering, Kunming University of Science and Technology, Kunming 650093, China*
[d] *Research Center for Analysis and Measurement, Kunming University of Science and Technology, Kunming 650093, China*

A R T I C L E   I N F O

A B S T R A C T

Single-atom catalysts have been extensively researched in electrocatalytic oxygen reduction and evolution reactions (ORR/OER) due to their tunable coordination environment. However, the linear scaling relationship (LSR) of oxygen intermediate adsorption energies imposes limitations in simultaneously enhancing ORR/OER. Herein, a unique asymmetrically coordinated FeN$_3$P$_1$ single-atom configuration coupled by Fe$_2$P nanoparticle is synthesized via a prefabricated Fe-N/P coordination strategy. The accentuated structural distortion induced by Fe$_2$P can effectively break the LSR, lowering the energy barriers for ORR/OER. Kinetically, a modulation of OH$^-$ concentration by Fe$_2$P on the catalytic interface was identified by finite element simulation and molecular dynamics simulation, which can positively facilitate ORR/OER kinetics. The obtained Fe$_2$P@FeN$_3$P$_1$-NC catalyst exhibits excellent bifunctional ORR/OER ($\Delta E = 0.65$ V) and a promising application in zinc-air battery. This work provides a valuable insight into simultaneous regulation of thermodynamic and kinetic behavior by tailored structure distortion and enriched surface ions for ORR/OER.

1. Introduction

The design of non-precious metal catalysts for oxygen reduction and evolution reactions (ORR/OER) is the key to promote the development and commercialization of new energy devices such as fuel cells and metal-air batteries [1–4]. Nitrogen-doped carbon materials anchored with transition metal catalysts (M-N-C), particularly Fe-N-C, have garnered significant attention and research interest due to their exceptional ORR performance [5–7]. The predominant structure of Fe-N-C is a single atom-dispersed with nitrogen-coordinated in a symmetrical planar quadrilateral known as FeN$_4$ [8,9]. In recent years, there has been a significant focus on improving the effectiveness of single atom sites through different approaches. These approaches involve manipulating the electronic structure of central metal atoms by exerting control over their coordination environment [10–12]. This can be achieved through direct coordination by heteroatoms or by introducing heteroatoms into carbon layers to establish long-range electronic interactions [13–17]. Other approaches involve increasing the density of single atom sites [18–20]; designing tailored physical structures to enhance the exposure

and utilization of active sites by augmenting the specific surface area [21–23]. Although these strategies have demonstrated remarkable ORR performance for most transition metal M-N-C catalysts, their OER activity remains limited. This limitation arises from the fact that solely manipulating the electronic structure based on a geometrically symmetric FeN$_4$ motif results in a linear scaling relationship (LSR) in adsorption energy of oxygen intermediates (e.g., O*, OH*, and OOH*) [24]. For instance, simultaneous increase in adsorption energies of both O* and OOH* involved in determining OER/ORR benefits ORR but impedes OER. Therefore, it is crucial to break this LSR by considering geometric and electronic structure perspectives in order to achieve highly active bifunctional catalysts for ORR/OER [25].

The electronegativity of the P atom is comparatively lower than that of N, while its atomic radius is larger. This characteristic enables it donates electrons and induce local structural distortions simultaneously. In most current research reports, P atoms are coordinated in the second shell of Fe or doped into a carbon substrate [26–29]. In such cases, the extent of structural distortion and electron transfer relies on the density and proximity of doped P atoms to the central metal Fe. However, if P

atom directly coordinate in the first shell with central metal Fe to form an asymmetric configuration (FeN$_3$P$_1$), it can more effectively introduce significant structural distortions at single iron atom site and help break the LSR [26], thus potentially improving both ORR/OER bifunctional performance.

Furthermore, aside from thermodynamic modulation, the role of kinetics is also significant in its influence on the catalytic reaction. One viable method in optimizing kinetics is the regulation of the ionic concentration of reactants at the catalytic interface. The regulation can be achieved by introducing components with excellent electrical conductivity, like metal phosphides, through the field-induced reagent concentration (FIRC) effect [30–33]. This effect can increase the reactant concentration and mass transfer efficiency, improving the reaction kinetics and ultimately enhancing the reaction performance.

Based on the above, the idea of introducing the P element to construct the asymmetric FeN$_3$P$_1$ single-atom sites coupled with the iron phosphide particles Fe$_2$P is proposed to optimize the thermodynamic and kinetic properties simultaneously with the aim of obtaining enhanced ORR/OER bifunctional performance.

To realize this idea, a prefabricated Fe-N/P coordination strategy is employed in this study to synthesize bifunctional catalyst consisting of single-atom FeN$_3$P$_1$ sites and Fe$_2$P nanoparticles. Density functional theory (DFT) calculations show that, in contrast to the planar tetrahedral structure of FeN$_4$, the introduction of P in FeN$_3$P$_1$ disrupts the symmetric arrangement and induces structural distortion at the single-atom site. Under the influence of Fe$_2$P particles, further structural distortion occurs, breaking the LSR and achieving an optimized oxygen intermediate adsorption energy that can benefit ORR/OER. Additionally, finite element simulation demonstrates that Fe$_2$P particles can induce stronger local electric fields to exert a surface ion concentration effect, while molecular dynamics simulation verifies their ability to increase reactant OH$^-$ ion concentration in OER and also can promote product OH$^-$ ion diffusion in ORR at the catalystic interface. Overall, the distortion of the local structure effectively breaking the LSR of oxygen intermediates' adsorption energy and simultaneously combines with the electric field-induced ion concentration effect to enhance ORR/OER performance. The resulting Fe$_2$P@FeN$_3$P$_1$-NC catalyst exhibits a half-wave potential of 0.88 V in ORR and an overpotential of only 300 mV at 10 mA cm^{-2} current density in OER, yielding an exceptionally low oxygen overpotential gap (ΔE) of merely 0.65 V for ORR/OER applications, which is much lower than that of the commercial Pt/C+RuO$_2$ catalysts (ΔE = 0.78 V), and ranks as one of the highest reported in the state-of-the-art for related Fe single-atom catalysts. Furthermore, it demonstrates a peak power density of 227.3 mW cm^{-2} along with decent long-term cycling stability when employed in zinc-air batteries. This study presents innovative concepts for designing bifunctional ORR/OER catalysts by considering thermodynamic and kinetic factors.

2. Experimental section

2.1. Chemicals and materials synthesis

2.1.1. Chemicals

1, 2-Cyclohexanediamine (cis-trans mixture, 99%) and 2-diphenyl-phosphinobenzaldehyde (analytical purity) were purchased from Macklin (Shanghai China). Ferric chloride hexahydrate (analytical purity) and dicyandiamide (analytical purity) were purchased from Aladdin (Shanghai China). Carbon black was CABOT BP2000 from USA. Commercial Pt/C catalyst (Johnson Matthey, 20 wt%) were purchased from Hesen (Shanghai China).

2.1.2. Synthesis of the organic ligand N$_2$P$_2$

The synthesis of N$_2$P$_2$ ligand was referred to previous report [34,35]. 1, 2-Cyclohexanediamine (3.8 mmol, 466 μL), 2-diphenylphosphinoben-zaldehyde (7.6 mmol, 2.2 g), and ethanol (120 mL) were refluxed under nitrogen atmosphere for 24 h. Following the process of cooling to

ambient temperature, the solvent was then eliminated by the employment of rotary evaporation, resulting in the acquisition of the light yellow N$_2$P$_2$ complex (Scheme 1).

2.1.3. Synthesis of catalysts

N$_2$P$_2$ ligand (114 mg), FeCl$_2$·4H$_2$O (30 mg) was mixed with ethanol (15 mL) and stirred for 30 min to fully dissolve. The mixed solution was subjected to a reflux reaction in the presence of a nitrogen environment at a temperature of 80 °C for a duration of 4 h. This reaction was carried out in order to achieve full coordination between the iron ions and the N$_2$P$_2$ ligands. Following the process of cooling to ambient temperature, the substance was combined with BP2000 (150 mg) and DCDA (6 g), and subsequently subjected to grinding until complete evaporation of ethanol occurred. The solid powder obtained was introduced into a tube furnace with a nitrogen environment. The temperature was gradually increased to 550 °C at a rate of 2.5 °C per minute and maintained for a duration of 2 h. Subsequently, the temperature was further increased to 800 °C at a rate of 5 °C per minute and kept for an additional 2 h. The obtained catalyst was named Fe$_2$P@FeN$_3$P$_1$-NC. The catalyst was pickled in 0.5 M H$_2$SO$_4$ solution to remove Fe$_2$P, and the obtained catalyst was named SA-FeN$_3$P$_1$-NC. The comparison catalyst Fe-NC was synthesized in the same way as Fe$_2$P@FeN$_3$P$_1$-NC, except that the N$_2$P$_2$ ligand was not added. The comparison catalyst NC was synthesized in the same way as Fe$_2$P@FeN$_3$P$_1$-NC, except that N$_2$P$_2$ ligand and FeCl$_2$·4H$_2$O were not added.

2.2. Electrochemical measurements

The methods of electrochemical testing were referred to previous published work [16] (see details in Supporting Information).

2.3. Theoretical simulation

2.3.1. DFT calculation methods

The spin-polarization DFT computations were conducted utilizing the generalized gradient approximation (GGA) and the Perdew-Burke-Ernzerhof (PBE) formulation within the CASTEP code [36,37]. The inclusion of Hubbard U corrections was undertaken in order to account for the on-site Coulomb repulsion experienced by d electrons. For Fe atoms, the U-J parameters were specifically adjusted at a value of 3.00. The planewave basis's kinetic cut-off energy was 450 eV. The perpendicular gap between vacuum layers within the structure measures 15 Å. Fe$_2$P modeling was performed with the most stable (001) surface as the active surface layer. Fe$_2$P@FeN$_3$P$_1$ was modeled using 5×5 graphite layer supercell with 2×2 Fe$_2$P supercell to construct a heterogeneous interface, and lattice matching parameters were chosen as average, with (U V θ) of (11.96 11.96 60°). The graphite layer and the upper two Fe$_2$P layers were kept relaxed and the remaining two layers were frozen during the structure optimization. The details of DFT calculations were referred to previously published work [16,38] (see details in Supporting Information).

2.3.2. Molecular dynamics simulations

Two solution models were constructed: a comparison solution box containing only FeN$_3$P$_1$, H$_2$O and KOH, and an experimental solution box containing Fe$_2$P, FeN$_3$P$_1$, H$_2$O and KOH. The comparison solution box contained 7 KOH and 393 H$_2$O molecules, while the Fe$_2$P solution box contained 10 KOH and 556 H$_2$O molecules. To simulate OER and ORR scenarios, electric fields in reverse directions (0 0 1 and 0 0 −1) were applied to the two boxes with potentials of 2 V and 0.8 V respectively. The Forcite module was used for all molecular dynamics (MD) simulations, and the COMPASS force field was applied to all simulations. The solution models were equilibrated in the NVT ensemble using the Berendsen barostat with a 0.1 ps decay for 20 ps and a Nose thermostat at 298 K [39,40]. After equilibration, the production runs were carried out in an NVT ensemble of 200 ps to ensure the solution system was in
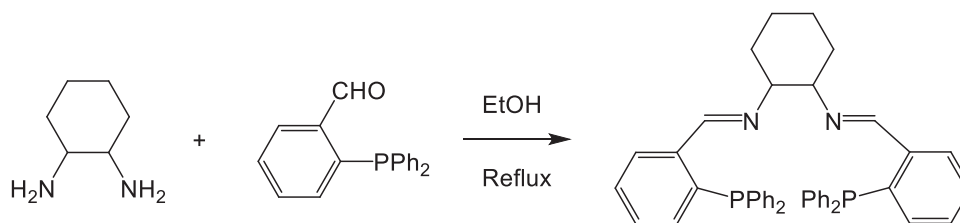
Scheme 1. Synthesis of the N$_2$P$_2$ ligand.

equilibrium [41].

2.3.3. Finite element method simulations

The finite element method (FEM) model was constructed with COMSOL Multiphysics as stationary. To simplify the model, both carbon nanoparticles and Fe$_2$P nanoparticles were simulated using a circular symmetric 2D model (Diameter: 20.0 nm). The electrolytes used in the ORR simulation were 0.1 M KOH, and 1.0 M KOH in the OER. The "Electrostatics" module and the "Three Times current distribution" module were used to simulate the electric field distribution. Free triangular meshes were used for all simulations. The electrical

conductivity of carbon nanoparticles and Fe$_2$P nanoparticles were set to 2.85 [42] and 3.33×10^5 [43], respectively. Specific bias voltages were applied to the solutions during the simulations (0.6 V for ORR and 1.6 V for OER). The Gouy–Chapman–Stern model was employed to simulate the behavior of the electrical double layer. The density of the hydroxide ion (OH$^-$) in the electrical double layer was examined using the "Transport of diluted species" module. The diffusion coefficients of the K$^+$ and OH$^-$ ions in H$_2$O were taken to be 2.14×10^{-9} and 7.02×10^{-9} m^2 s^{-1} [31], respectively. The relative tolerance of the MUMPS solver is 0.001.
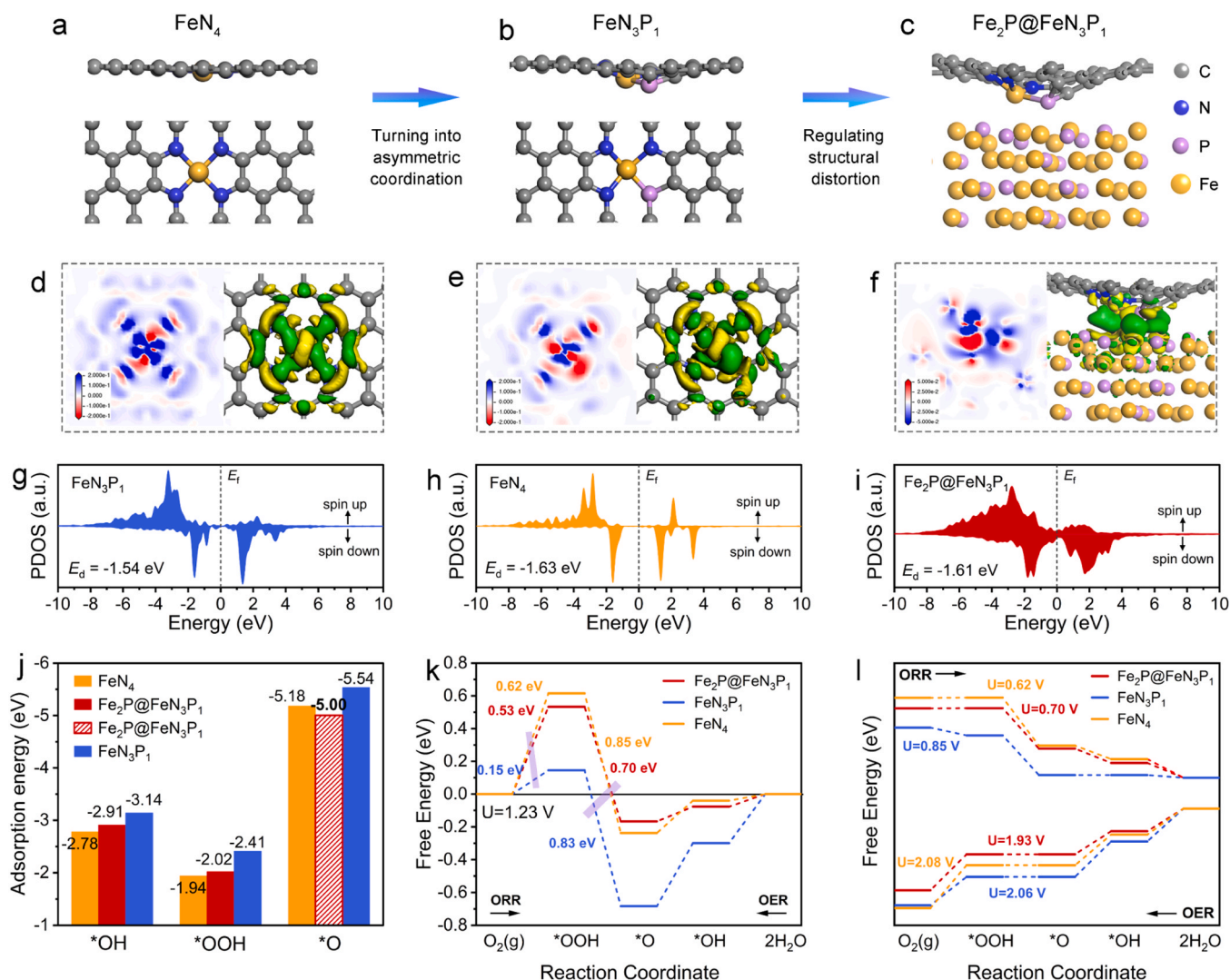

Fig. 1. (a) Side-view and top-view of the optimal FeN$_4$ model, (b) side-view and top-view of the optimal FeN$_3$P$_1$ model, (c) side-view of the optimal Fe$_2$P@FeN$_3$P$_1$ model. (d) Density difference top-view slice and isosurfaces display of FeN$_4$, (e) density difference top-view slice and isosurfaces display of FeN$_3$P$_1$, (f) density difference side-view slice and isosurfaces display of Fe$_2$P@FeN$_3$P$_1$. Calculated PDOS curves of Fe-3d orbital for (g) FeN$_4$, (h) FeN$_3$P$_1$, (i) Fe$_2$P@FeN$_3$P$_1$. (j) Adsorption energies of oxygen-containing intermediates. Free-energy diagram of ORR and OER at (k) 1.23 V and (l) specified potentials.

3. Results and discussion

3.1. Theoretical simulations

As mentioned previously, we speculate that the $Fe_2P@FeN_3P_1$ structure, formed by coupling Fe_2P with asymmetrically coordinated FeN_3P_1 in contrast to the geometrically symmetric FeN_4 single-atom site, may be able to break the linear scaling relationship of the adsorption energy of O* /OOH* in the ORR/OER process from a thermodynamic point of view [26], which is conducive to the simultaneous improvement of the bifunctional performance. Additionally, from a kinetic standpoint, due to the excellent electrical conductivity of Fe_2P particles, the coupled Fe_2P is capable of modulating the ion concentration at the catalytic interface by FIRC through the electric field strength induced by Fe_2P, potentially enhancing the reaction kinetics of ORR/OER simultaneously. In order to verify these two speculations, theoretical simulations were performed in this work from thermodynamic and kinetic perspectives, respectively.

3.1.1. DFT to probe thermodynamic feasibility

In order to investigate the thermodynamic advantages of asymmetrically coordinated FeN_3P_1 single-atom sites as well as Fe_2P coupled, DFT is employed here. Models containing FeN_4, FeN_3P_1 single-atom sites, and FeN_3P_1 single-atom sites coupled with Fe_2P are built as shown in Fig. 1a-c. It can be seen that in the FeN_3P_1 model, localized deformation and stretching are imposed on the graphitic carbon layer due to the substitution of P for N coordination. In the $Fe_2P@FeN_3P_1$ model, the local distortion is further deepened under the induction of Fe_2P. The specific bond length changes are shown in Table S1, where the P coordination stretches the Fe-N bond lengths and the stretching effect is further enhanced under the influence of Fe_2P. The differential charge density results in Fig. 1d-f also demonstrate the breaking of the planar tetragonal symmetric structure of the conventional FeN_4 by P coordination, resulting in the formation of an asymmetric electron distribution structure (Figs. S1-S3). From Fig. 1f, it is evident that electron transfer occurs between Fe_2P and FeN_3P_1 single-atom sites, indicating the electron-inducing effect of Fe_2P on FeN_3P_1 single-atom sites. On the other hand, due to the electron-donating property of P, the valence state of the center metal Fe in the FeN_3P_1 model is lower relative to that of the conventional FeN_4, and the coupling of Fe_2P leads to a further electron transfer and a further decrease in the charge of Fe (Table S2). This alteration in electronic structure exerts a direct influence on the position of the d-band center, as depicted in Fig. 1g-i, $Fe_2P@FeN_3P_1$ exhibit higher d-band centers compared to the conventional FeN_4 configuration, indicating an enhanced oxygen binding capability [44]. Moreover, Fig. 1j presents the calculated results for the adsorption energy of oxygen-containing intermediates, highlighting that $Fe_2P@FeN_3P_1$ exhibits higher *OOH and *OH binding energies than that of FeN_4, which is favorable for the first step in ORR and OER, respectively. Meanwhile, it is meaningful to note that there is no enhancement of the *O adsorption strength, and the weakened O* adsorption strength favors the coupling of O-O bonds in the OER process. This suggests that the $Fe_2P@FeN_3P_1$ structure breaks the LSR of the adsorption strength for oxygenated intermediates, which in turn thermodynamically contributes to the excellent ORR/OER catalytic performance.

Further, the Gibbs free energy changes were calculated for each step of the ORR/OER at an equilibrium potential of 1.23 V (Fig. 1k) [45–48]. Calculations show that FeN_4 possesses an energy barrier of 0.62 eV at the rate-determining step (* → *OOH) of the ORR, whereas $Fe_2P@$-FeN_3P_1 possesses a lower energy barrier of 0.53 eV at this step, which is attributed to the higher *OOH adsorption energy of this structure. During the OER process, the coupling of O-O bonds (*O → *OOH) constitutes the rate-determining step, and $Fe_2P@FeN_3P_1$ exhibits the lowest reaction energy barrier at this step. This demonstrates that the weakening of the O* binding energy due to structural stretching and distortion in $Fe_2P@FeN_3P_1$ favors the O-O bond coupling and thus

thermodynamically facilitates the OER. Fig. 1l shows the critical potentials that need to be imposed for the three structural models to be thermodynamically feasible for ORR and OER, respectively, and the result is in agreement with Fig. 1k, which further suggests that $Fe_2P@FeN_3P_1$ has better bifunctional ORR/OER thermodynamic advantages. Notably, the Gibbs free energy changes (Fig. S11) of the ORR/OER for Fe_2P are also calculated in order to investigate whether Fe_2P is the active site. The results show that there is a significant potential barrier for each step of the reaction history, which can be used to determine that the main active site is the FeN_3P_1 single-atom site rather than Fe_2P in the $Fe_2P@FeN_3P_1$ structure.

3.1.2. Dynamics simulation

Reaction kinetics is a crucial aspect when deciding catalytic processes. Unfortunately, this factor is often overlooked in most catalyst design. Effective strategies for improving reaction kinetics include reducing charge transfer resistance, increasing reactant concentration, and promoting product diffusion at the reaction interface. It is possible to hypothesize that by introducing components with excellent electrical conductivity, such as Fe_2P metal particles, and making adjustments to the concentration of reactant ions at the catalytic interface through FIRC, it could potentially improve the reaction kinetics.

To verify this hypothesis, Fe_2P particle coupling to carbon was modelled by finite element simulation to analyse the resulting variation in electric field strength at the catalyst surface [31,42]. Fig. 2a-d show that after the coupling of Fe_2P particles, the catalyst surface exhibits a stronger electric field strength at both the ORR and OER polarization potentials. The impact of hydroxide ion concentration on the surface of the $Fe_2P@FeN_3P_1$ catalyst was explored through molecular dynamics simulations. It is important to note that in the alkaline system, OH^- is not only a product of ORR but also a reactant for OER due to the inverse reaction, where the ORR process is: $O_2 + 2H_2O + 4e^- \rightarrow 4OH^-$. Fig. 2e-f and Fig. S12 display the simulation snapshots under the ORR and OER potentials. The findings indicate that, in the ORR process, the OH^- concentration on the surface of $Fe_2P@FeN_3P_1$ catalyst is lower to that of FeN_3P_1 catalyst, implying that the coupling of Fe_2P facilitates the diffusion of product OH^- (Fig. 2g). Conversely, there was an occurrence of OH^- aggregation on the surface of $Fe_2P@FeN_3P_1$ in the OER process, with the amount of aggregation being considerably more substantial than that of FeN_3P_1 (Fig. 2h). The calculations indicated that Fe_2P particles enhanced product diffusion during the ORR process and OH^- aggregation during the OER process at their respective reduction and oxidation potentials. Additionally, finite element simulations were performed to calculate the ion concentration distribution and the results (Fig. S13) were consistent with those of the above molecular dynamics simulations. This indicates that Fe_2P can modulate the surface ion concentration, which is beneficial for the reaction kinetics.

3.2. Synthesis and structural characterization of catalysts

Based on the above calculations, the bifunctional catalysts with FeN_3P_1 single-atom sites coupled to Fe_2P have a theoretical foundation. Then a synthetic strategy of prefabricated Fe-N/P coordination is proposed. The synthesis process is illustrated in Fig. 3a. The N_2P_2-type organic complex synthesized via the Mannich reaction functions as a quadridentate ligand with dual nitrogen and dual phosphorus atoms (Scheme 1). The structural confirmation of N_2P_2 ligand was achieved through high-resolution mass spectrometry (Fig. S15). The robust coordination between metal ions and N_2P_2 ligands facilitates the immobilization and dispersion of iron ions within carbon-based materials by nitrogen and phosphorus [34,35,49–51], thereby providing a distinctive coordination architecture for the formation of N, P-coordinated single-atom iron site coupled with Fe_2P nanoparticles during high-temperature pyrolysis. XRD analysis reveals that the material synthesized through this approach contain a Fe_2P phase, which was subsequently eliminated after acid washing (Fig. S16), leaving only two
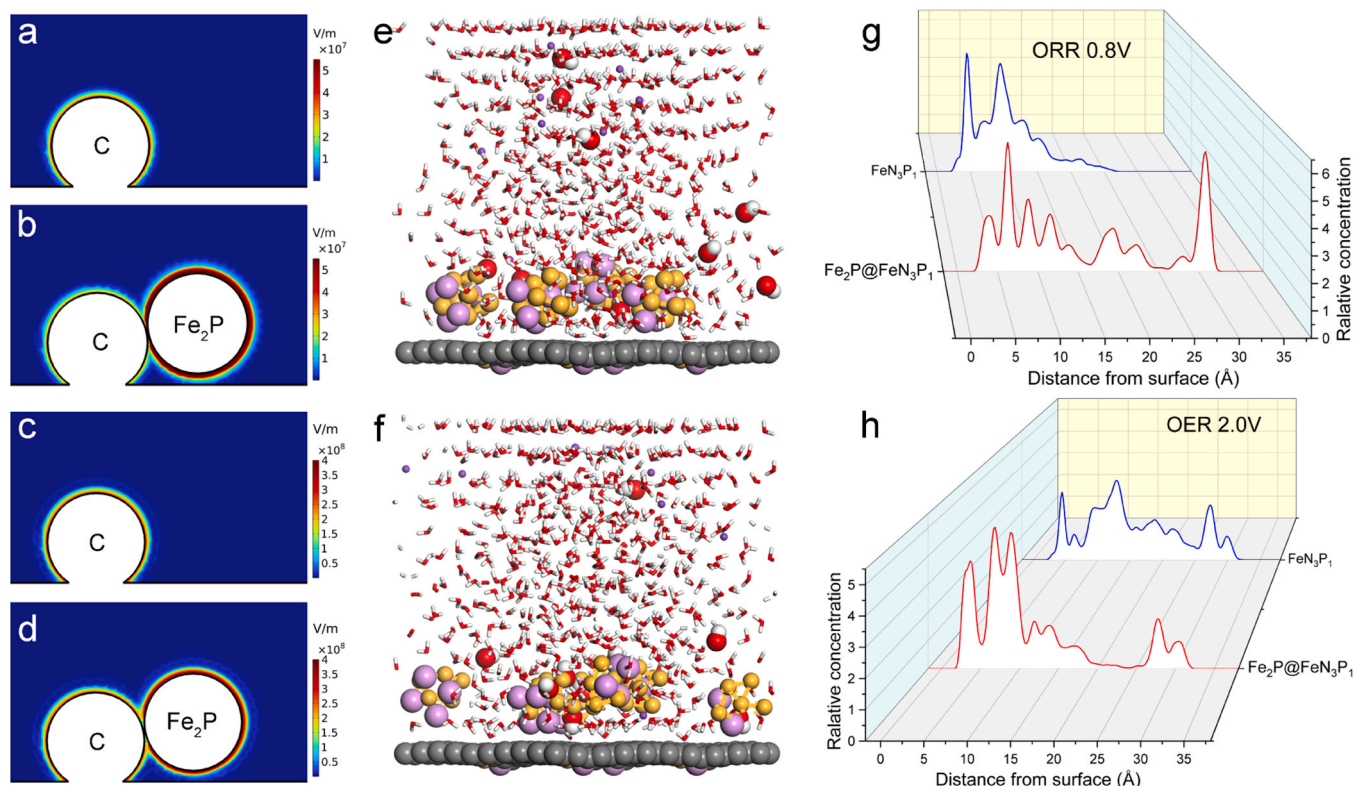
Fig. 2. The electric field intensity of (a) carbon nanoparticle and (b) carbon nanoparticle coupled with Fe_2P nanoparticle under ORR. The electric field intensity of (c) carbon nanoparticle and (d) carbon nanoparticle coupled with Fe_2P nanoparticle under OER. Molecular dynamics simulation snapshots of $Fe_2P@FeN_3P_1$ under (e) ORR and (f) OER. The calculated relative OH^- concentration at the surface of FeN_3P_1 and $Fe_2P@FeN_3P_1$ under (g) ORR and (h) OER.

distinct carbon peaks at 26° and 44° corresponding to the (002) and (101) crystal planes of graphite carbon. SEM characterization of $Fe_2P@FeN_3P_1$-NC and SA-FeN_3P_1-NC demonstrate that carbon nanoparticles were retained, exhibiting an evident stacked yet independent morphology (Fig. S17). BET analysis indicates that $Fe_2P@FeN_3P_1$-NC possesses a porous structure with a large specific surface area (Fig. S18), facilitating exposure of active sites. Furthermore, the high values of I_D/I_G in the Raman results (Fig. S19) indicate the existence of a significant number of defects in the carbon substrate [52,53], which come from the incomplete graphitization of C_3N_4 generated by the decomposition of dicyandiamide [54].

The transmission electron microscopy (TEM) results demonstrate the distribution of metal nanoparticles within the carbon material of $Fe_2P@FeN_3P_1$-NC, as shown in Fig. 3b. As can be seen from Fig. S20, the Fe_2P particles are loaded on carbon carriers, and the magnification image of individual Fe_2P particles shows that the Fe_2P particles are partially wrapped with single or multiple layers of graphene. It indicates that the position between Fe_2P particles and graphite layers is interdependent. Additionally, aberration-corrected high-angle annular dark-field scanning transmission electron microscopy (HAADF-STEM) imaging reveals the presence of individual metal atoms on the carbon material, exhibiting significantly higher contrast compared to the carbon substrate, as depicted in Fig. 3c-d. Furthermore, elemental mapping (Fig. 3e) confirms a homogeneous distribution of carbon and nitrogen elements, indicating nitrogen-doped carbon. The spatial arrangement of phosphorus and iron elements corresponds well with XRD and HAADF-STEM results, suggesting coexistence of Fe_2P nanoparticles and single atomic FeN_3P_1 sites. TEM (Fig. 3f), HAADF-STEM (Fig. 3g-h) and elemental mapping (Fig. 3i) for SA-FeN_3P_1-NC indicate an absence of Fe_2P nanoparticles, with iron atoms dispersed in a single atomic form within the nitrogen-doped carbon substrate. The Fe single atoms in Fig. 3g are marked with circles [55,56]. The XPS technique was employed for further characterization of the chemical states of various

elements in the material. Fig. S21 illustrates that N predominantly exists as pyridinic N, Fe-N_x, pyrrolic N, graphitic N, and oxidized N [57,58], indicating the presence of single-atom Fe coordinated with N. The P 2p and Fe 2p XPS results depicted in Fig. S22 demonstrate that P doping within the carbon substrate in both $Fe_2P@FeN_3P_1$-NC and SA-FeN_3P_1-NC, and confirms the existence of Fe_2P in $Fe_2P@FeN_3P_1$-NC [59,60].

In view of the presence of individual atoms in both $Fe_2P@FeN_3P_1$-NC and SA-FeN_3P_1-NC, it can be inferred from the synthesis process that these Fe single atoms are of the same type. To further investigate the precise chemical state and coordination environment of the Fe single atoms, synchrotron radiation characterization was employed to analyze the Fe element in SA-FeN_3P_1-NC. The E-space analysis depicted in Fig. 4a indicates that the valence state of Fe in SA-FeN_3P_1-NC ranges between 0 and +2, while in FePc it ranges between +2 and +3. This suggests a distinct chemical environment for Fe in SA-FeN_3P_1-NC compared to the Fe-N_4 observed in FePc, with a relatively electron-rich state for Fe. This is attributed to the electron-donating properties of the P atom, and the change in valence is consistent with the DFT calculations. The R-space results displayed in Fig. 4b reveal no evidence of any interatomic bonds involving iron within SA-FeN_3P_1-NC, confirming that iron exists as isolated single atoms, consistent with XRD and aberration-corrected findings. The primary peak observed at approximately 1.53 Å is similar to that seen in FePc due to backscattering between iron and nitrogen atoms. Wavelet transform analysis shown in Fig. 4c clearly demonstrates a different coordination environment for iron in SA-FeN_3P_1-NC compared to other standard samples; there are no vibration peaks corresponding to iron–iron bonds; moreover, its strongest vibration peak position is close but distinct from those corresponding to Fe-O or Fe-N bonds, suggesting a similar yet not identical coordination environment for this specific atom. The fitting result obtained from near-edge absorption spectroscopy indicates combined coordination by nitrogen and phosphorus with respective coordination numbers being 3.0
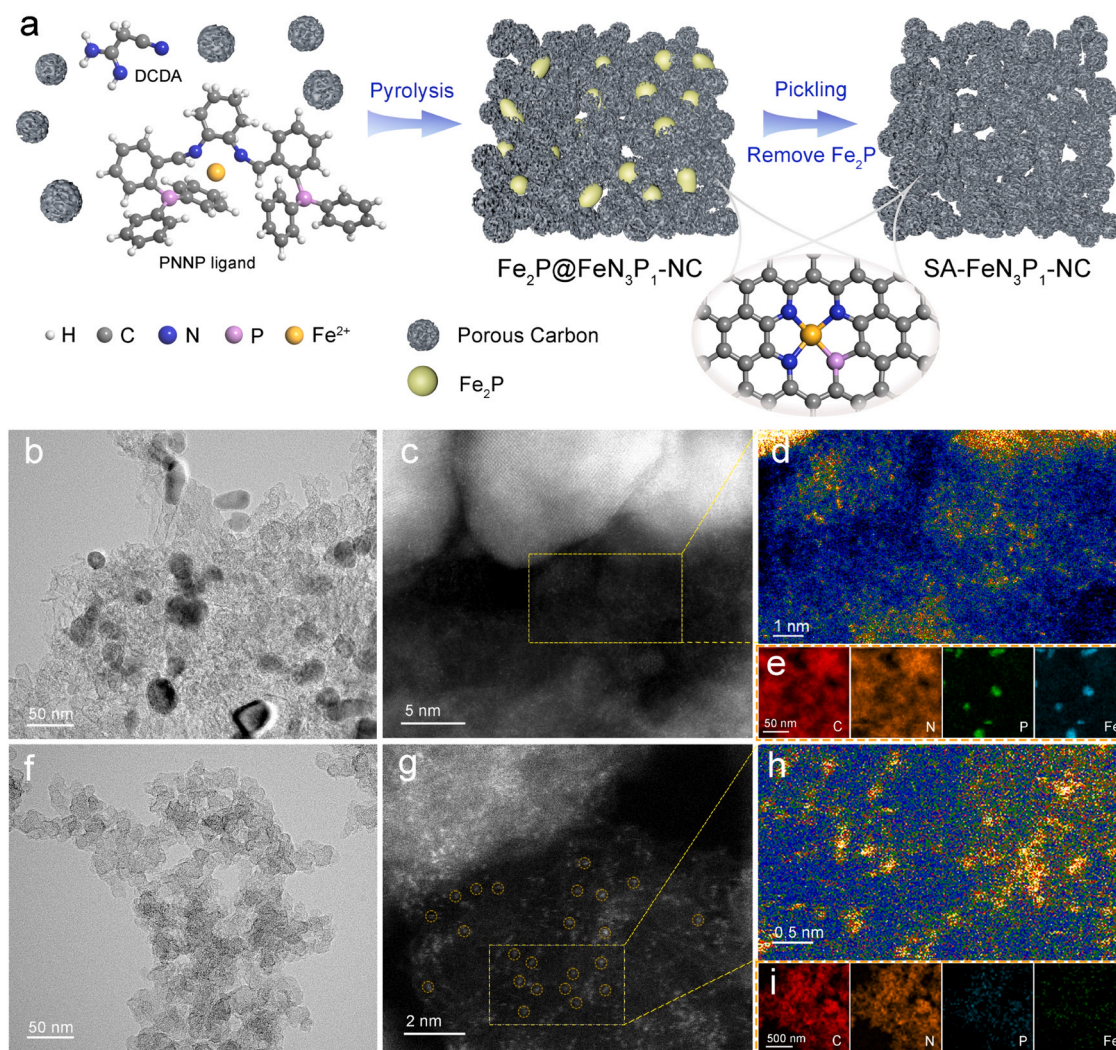
Fig. 3. (a) Schematic illustration of the synthesis of $Fe_2P@FeN_3P_1$-NC and SA-FeN_3P_1-NC. (b) TEM image of $Fe_2P@FeN_3P_1$-NC. (c) HAADF-STEM image of $Fe_2P@FeN_3P_1$-NC and (d) enlargement of the corresponding area. (e) EDS elemental mapping of $Fe_2P@FeN_3P_1$-NC. (f) TEM image of SA-FeN_3P_1-NC. (g) HAADF-STEM image of SA-FeN_3P_1-NC and (h) enlargement of the corresponding area. (i) EDS elemental mapping of SA-FeN_3P_1-NC.

and 1.1 for this particular structure, as show in Fig. 4d-e and Table S3. Based on these findings, the coordinated environment of the monatomic iron in SA-FeN_3P_1-NC can reasonably assign as FeN_3P_1.

3.3. Electrocatalytic performance

The obtained catalyst was utilized for ORR and OER. As shown in Fig. 5a, the ORR LSV test demonstrates that $Fe_2P@FeN_3P_1$-NC exhibits superior performance with an onset potential of 1.00 V and a half-wave potential of 0.88 V, surpassing SA-FeN_3P_1-NC (0.85 V), Fe-NC (0.83 V), and commercial Pt/C (0.84 V). Additionally, the kinetic current density of $Fe_2P@FeN_3P_1$-NC is found to be the highest among all tested catalysts (Fig. 5b), indicating its excellent kinetic performance. The normalized current density by electrochemical surface area (Fig. 5c) reveals that $Fe_2P@FeN_3P_1$-NC displays optimal performance compared to SA-FeN_3P_1-NC, suggesting a significant enhancement in catalytic intrinsic activity attributed to the presence of Fe_2P particles. Rotating ring-disk electrode (RRDE) analysis was employed to explore the pathway and mechanism of ORR (Fig. 5d), revealing that $Fe_2P@FeN_3P_1$-NC exhibits minimal H_2O_2 yield and approaches a nearly four-electron reaction pathway; the lower hydrogen peroxide production indicates reduced generation of oxygen radicals. It can be beneficial for catalyst stability and durability in practical battery applications.

The OER activity of the catalyst under either 1.0 M KOH or 0.1 M KOH was investigated simultaneously. In Fig. 5e, $Fe_2P@FeN_3P_1$-NC exhibits a potential of 1.55 V and an overpotential of only 320 mV at a current density of 50 mg cm^{-2} under 1.0 M KOH, outperforming the commercial RuO_2 catalyst with a potential of 1.63 V (η = 400 mV), while SA-FeN_3P_1-NC presents a potential of 1.60 V (η = 370 mV). The Tafel slope calculation results (Fig. 5f) demonstrate that $Fe_2P@FeN_3P_1$-NC possesses the smallest Tafel slope, measuring only 49.4 mV dec^{-1}, indicating its outstanding kinetic performance. Conversely, SA-FeN_3P_1-NC exhibits a Tafel slope of 64.0 mV dec^{-1} and RuO_2 has one as high as 96.6 mV dec^{-1}. The performance characterization conducted in 0.1 M KOH (Fig. S28a) also showcases the outstanding performance of $Fe_2P@FeN_3P_1$-NC. Electrochemical impedance spectroscopy (EIS) Nyquist plots obtained in Fig. 5g and Fig. S28b indicate that $Fe_2P@$-FeN_3P_1-NC displayed lower electrochemical impedance compared to SA-FeN_3P_1-NC, which is consistent with previous theoretical calculations on band structure (Fig. S5); due to coupling with Fe_2P, $Fe_2P@$-FeN_3P_1-NC possesses the narrowest band gap and exhibits conductor-like characteristics as well as minimal impedance.

The stability of $Fe_2P@FeN_3P_1$-NC in both the ORR and OER was evaluated using chronoamperometry method, as shown in Fig. 5h-i. The results demonstrate the exceptional stability of $Fe_2P@FeN_3P_1$-NC in ORR, with a final current density retention of 86% after operating at a
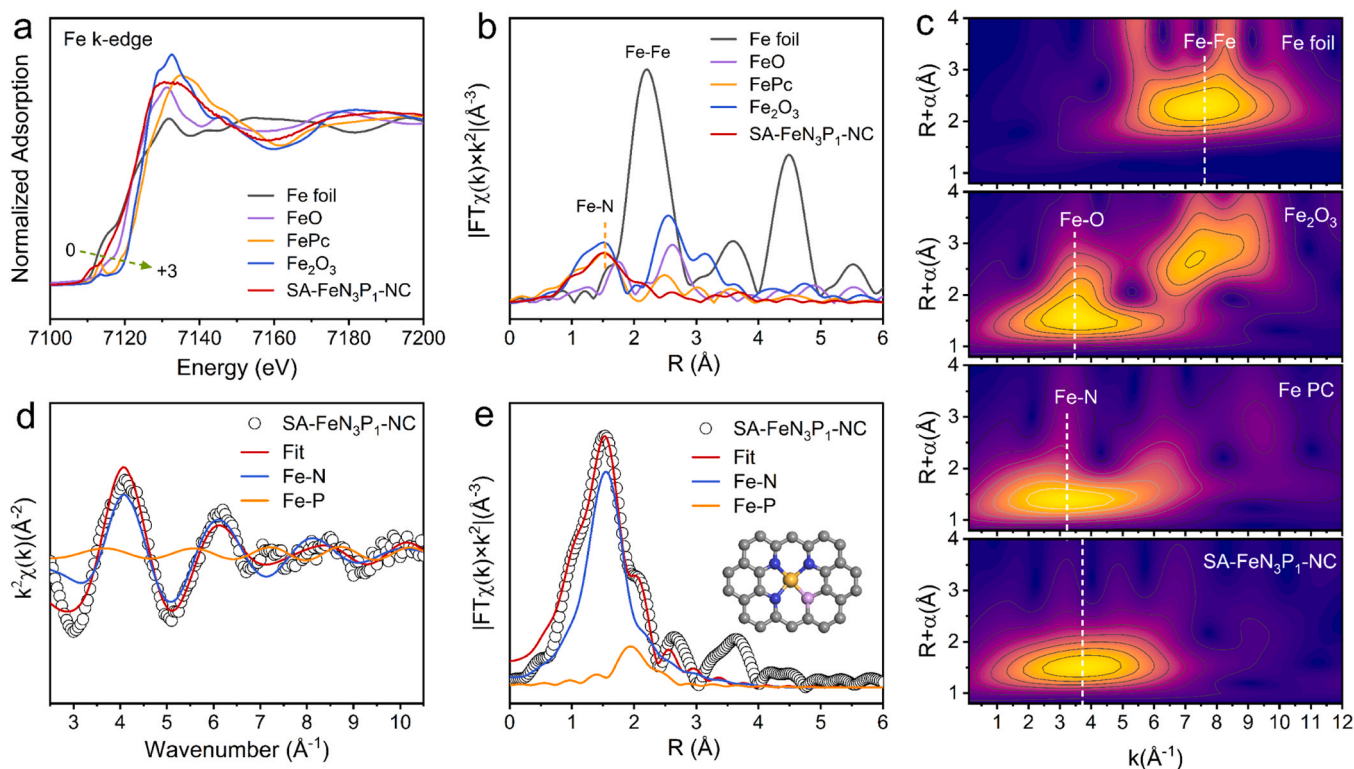
Fig. 4. XAFS measurements of SA-FeN$_3$P$_1$-NC. (a) Fe K-edge XANES spectra. (b) k^2-weighted Fourier transform extended X-ray absorption fine structure (EXAFS) spectra. (c) EXAFS WT analysis. EXAFS fitting curves in the (d) k-space and (e) R-space.

potential of 0.82 V for 20,000 s, which is significantly higher than that of the commercial Pt/C catalyst (61%). Moreover, it exhibits outstanding stability in OER as evidenced by negligible loss in current density after a testing period of 1000 min, experiencing only a slight decrease of 0.05%. To investigate the stability of Fe$_2$P@FeN$_3$P$_1$-NC under industrial conditions, chronopotentiometry was applied at the current density of 500 mA cm^{-2}. As shown in Fig. S29, Fe$_2$P@FeN$_3$P$_1$-NC showed excellent stability, indicating its commercial potential. The morphology of the Fe$_2$P@FeN$_3$P$_1$-NC catalyst was further characterized after a long-term chronopotentiometry OER test to probe the structural evolution [61]. As depicted in Fig. S30, the morphology of the catalyst is maintained after the long-term test as a noticeable accumulation of carbon particles. Additionally, XRD analysis (Fig. S31) reveals that the larger Fe$_2$P particles in Fe$_2$P@FeN$_3$P$_1$-NC are shedding, leaving only faint characteristic peaks of Fe$_2$P (marked by diamond-shaped squares in Fig. S31), indicating the presence of smaller Fe$_2$P particles. Based on the OER performance depicted in Fig. S29, it can be found that the shedding of Fe$_2$P particles does not significantly impact the stability, thereby suggesting that the FeN$_3$P$_1$ single atomic site serves as the primary active site in the catalyst. This is consistent with the conclusion of the theoretical calculations.

Typically, the potential gap between the potential at 10 mA cm^{-2} in OER and the half-wave potential in ORR at the same electrolyte is employed for assessing the bifunctional catalytic performance [62]. As illustrated in Fig. 5j and Table S5, Fe$_2$P@FeN$_3$P$_1$-NC exhibits an impressively low ΔE value of 0.65 V, that ranks as one of the highest reported in the state-of-the-art for related Fe single-atom catalysts (Table S6), highlighting its exceptional bifunctional oxygen electrocatalytic performance.

On the other hand, The ORR and OER performance of Fe$_2$P@FeN$_3$P$_1$-NC and SA-FeN$_3$P$_1$-NC were explored at different OH$^-$ concentrations. The performance of Fe$_2$P@FeN$_3$P$_1$-NC showed a smaller change compared to SA-FeN$_3$P$_1$-NC, as demonstrated in Figs. S32 and S33. This experimental result is consistent with the conclusions of the previous

theoretical simulations. The presence of Fe$_2$P particles promotes OH$^-$ diffusion in the ORR, as shown in Fig. S32e. As the OH$^-$ concentration increases, the attenuation of Fe$_2$P@FeN$_3$P$_1$-NC properties is less than that of SA-FeN$_3$P$_1$-NC. However, in OER, Fe$_2$P particles induce OH$^-$ aggregation, resulting in less attenuation of Fe$_2$P@FeN$_3$P$_1$-NC properties than SA-FeN$_3$P$_1$-NC as the OH$^-$ concentration decreases (Fig. S33c). This reflects the role of Fe$_2$P in optimizing the catalytic performance by regulating the OH$^-$ concentration at the catalytic interface.

3.4. Application in zinc-air battery

Zinc-air batteries (Fig. 6a) were employed to validate the catalytic performance of Fe$_2$P@FeN$_3$P$_1$-NC in practical devices. As depicted in Fig. 6b, when Fe$_2$P@FeN$_3$P$_1$-NC is utilized at the air electrode side, it exhibits an open circuit voltage of 1.50 V, surpassing that of the commercial Pt/C+RuO$_2$ (1.47 V), which indicating enhanced reversibility within the assembled battery system. Moreover, Fe$_2$P@FeN$_3$P$_1$-NC demonstrates a remarkable peak power density of 227.3 mW cm^{-2}, significantly outperforming commercial Pt/C (122.0 mW cm^{-2}) as illustrated in Fig. 6c, thus highlighting its exceptional discharge capability. The discharge curves at various current densities (Fig. 6d) further confirm the superior discharge ability and stability of Fe$_2$P@FeN$_3$P$_1$-NC. Additionally, cycle stability tests (Fig. 6e) reveal that compared to commercial Pt/C+RuO$_2$, Fe$_2$P@FeN$_3$P$_1$-NC exhibits lower charge-discharge potential gap and excellent long-term cycle stability with a round-trip efficiency exceeding 55% over an extended duration; thereby validating its outstanding application performance for ORR/OER in practical devices and indicating its potential for real-world applications.

4. Conclusion

In summary, an asymmetric FeN$_3$P$_1$ single-atom site coupled by Fe$_2$P nanoparticle was synthesized elaborately for efficient electrocatalytic ORR and OER. Excellent activity toward ORR/OER with a potential gap
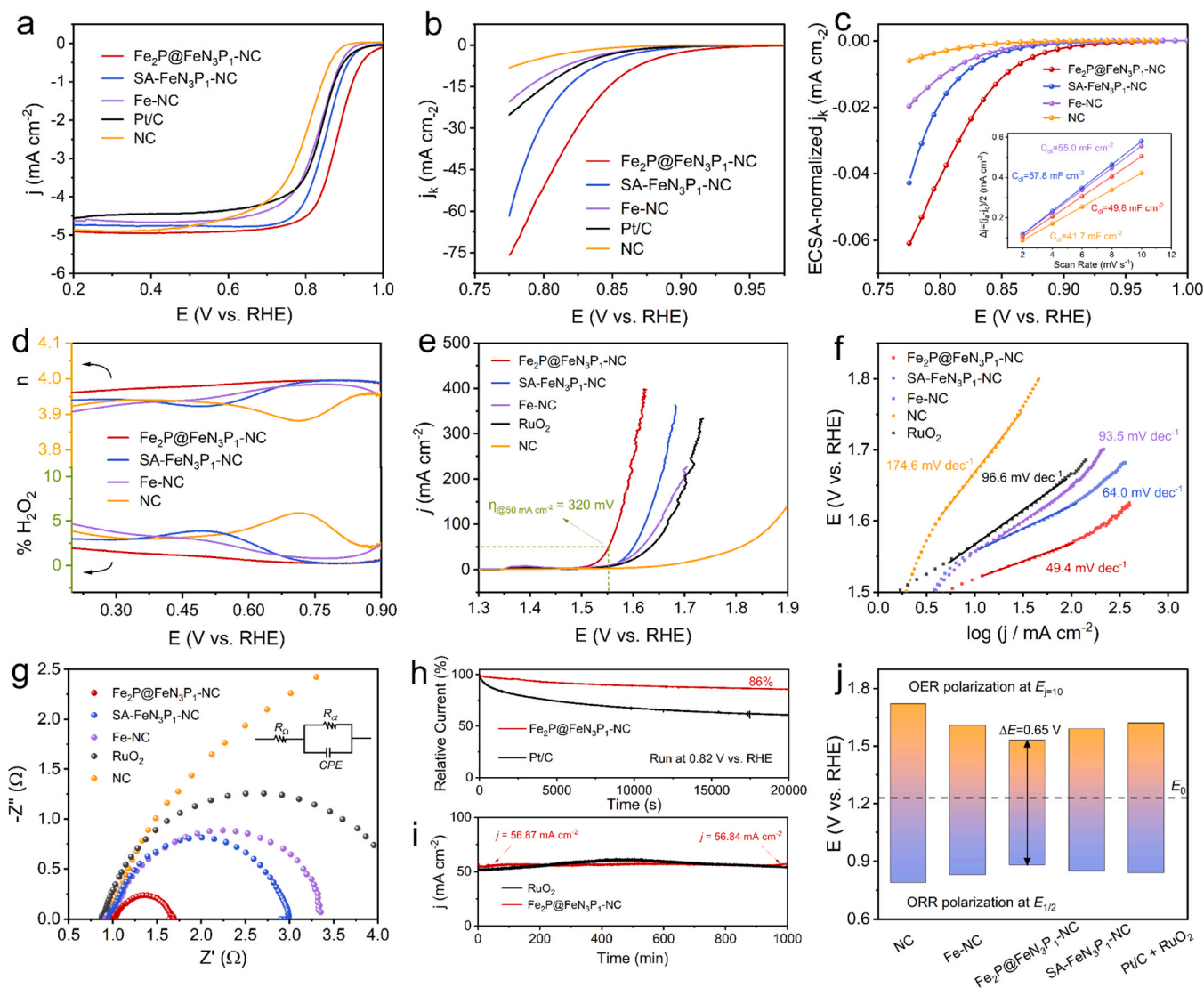
Fig. 5. (a) ORR LSV in O_2-saturated 0.1 M KOH solution at 1600 rpm. (b) Kinetic current density. (c) ECSA-normalized kinetic current density and the capacitive currents versus scan rates at 1.1 V versus RHE (inset). (d) Electron transfer number and the hydrogen peroxide yield obtained from RRDE test. (e) OER LSV curves in 1.0 M KOH with iRs compensation. (f) Tafel plots of OER. (g) Nyquist plots at 0.55 V vs. Ag/AgCl in 1.0 M KOH. (h) ORR Chronoamperometric measurement of $Fe_2P@FeN_3P_1$-NC and Pt/C. (i) OER Chronoamperometric measurement of $Fe_2P@FeN_3P_1$-NC and RuO_2. (j) Histogram comparisons of $E_{j=10}$ for OER and $E_{1/2}$ for ORR in 0.1 M KOH ($\Delta E = E_{j=10} - E_{1/2}$).

as small as 0.65 V is achieved in 0.1 M KOH. The assembled Zn-air battery using $Fe_2P@FeN_3P_1$-NC as the cathode exhibits a peak power density of 227.3 mW cm^{-2} and excellent long-term stability. The DFT calculations reveal that the structural distortion of asymmetric FeN_3P_1 single-atom sites is significantly amplified by the induction effect of Fe_2P, leading to a deviation from the LSR for adsorption energy of *O and *OOH. Consequently, this peculiarity confers dual benefits for ORR and OER. In terms of kinetics, molecular dynamics simulations and finite element simulations demonstrate that the presence of Fe_2P particles generates a higher electric field intensity, thereby augmenting the concentration of reactant ions and promoting the diffusion of products at the catalyst surface. Hence, this study presents an effective strategy and valuable insights for fabricating efficient ORR/OER catalysts from both thermodynamic and kinetic perspectives.

CRediT authorship contribution statement

Xu Mingli: Writing – review & editing, Supervision, Resources, Funding acquisition. **Zhu Enze:** Writing – original draft, Investigation, Formal analysis, Data curation, Conceptualization. **Shi Chaoyang:** Visualization, Formal analysis. **Yu Jie:** Resources, Methodology. **Jin Haodong:** Visualization, Conceptualization. **Zhou Linxiang:** Investigation, Data curation. **Yang Xikun:** Data curation, Conceptualization.

Declaration of Competing Interest

The authors declare the following financial interests/personal relationships which may be considered as potential competing interests: Mingli Xu reports financial support was provided by Major Special Project of Yunnan Province. Mingli Xu reports financial support was provided by Natural Science Foundation of Yunnan Province. Mingli Xu reports financial support was provided by Analysis and Testing Foundation of Kunming University of Science and Technology. Enze Zhu reports financial support was provided by Analysis and Testing Foundation of Kunming University of Science and Technology.
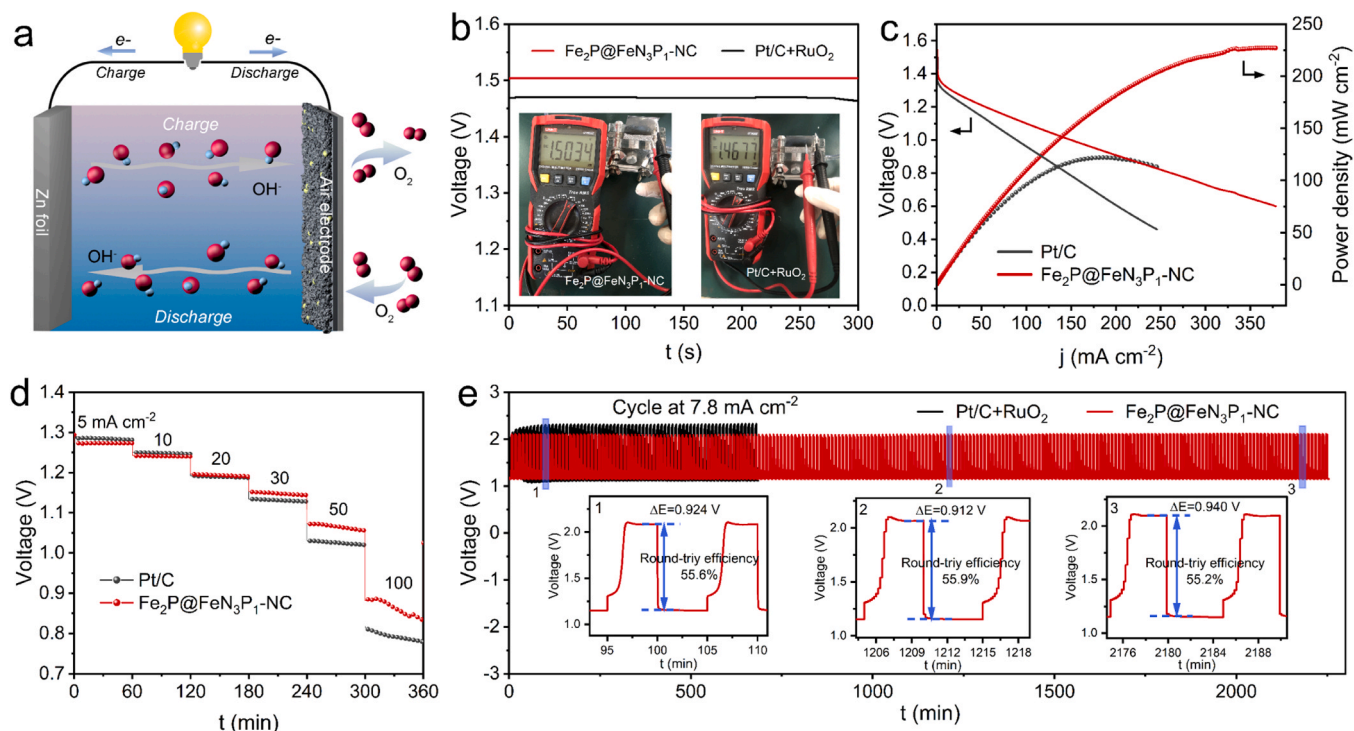
Fig. 6. ZAB test using $Fe_2P@FeN_3P_1$-NC or Pt/C+RuO_2 as the air electrode. (a) ZAB schematic, (b) digital images of output circuit voltage and open-circuit plots, (c) discharge polarization curves and corresponding power densities, (d) the discharge platforms at various current densities, (e) charge-discharge cycling stability curves.

Data Availability

Data will be made available on request.

Acknowledgements

Appendix A. Supporting information

Supplementary data associated with this article can be found in the online version at doi:10.1016/j.apcatb.2024.123796.

References

[1] X. Zhang, D. Xue, S. Jiang, H. Xia, Y. Yang, W. Yan, J. Hu, J. Zhang, Rational confinement engineering of MOF-derived carbon-based electrocatalysts toward CO_2 reduction and O_2 reduction reactions, InfoMat 4 (2022), https://doi.org/10.1002/inf2.12257.

[2] S. Jin, O. Allam, S.S. Jang, S.W. Lee, Covalent organic frameworks: design and applications in electrochemical energy storage devices, InfoMat 4 (2022), https://doi.org/10.1002/inf2.12277.

[3] Y. Du, B. Li, G. Xu, L. Wang, Recent advances in interface engineering strategy for highly-efficient electrocatalytic water splitting, InfoMat 5 (2023), https://doi.org/10.1002/inf2.12377.

[4] J. Wang, X. Liu, L. Li, R. Liu, Y. Liu, C. Wang, Z. Lv, W. Yang, X. Feng, B. Wang, Heterogeneous assembling 3D free-standing Co@carbon membrane enabling efficient fluid and flexible zinc-air batteries, Nano Res. 16 (2023) 9327–9334, https://doi.org/10.1007/s12274-023-5553-x.

[5] Z. Shi, W. Yang, Y. Gu, T. Liao, Z. Sun, Metal-nitrogen-doped carbon materials as highly efficient catalysts: progress and rational design, Adv. Sci. 7 (2020) 2001069, https://doi.org/10.1002/advs.202001069.

[6] X. Lu, Y. Li, D. Dong, Y. Wan, R. Li, L. Xiao, D. Wang, L. Liu, G. Wang, J. Zhang, M. An, P. Yang, Coexisting Fe single atoms and nanoparticles on hierarchically porous carbon for high-efficiency oxygen reduction reaction and Zn-air batteries, J. Colloid Interface Sci. 653 (2024) 654–663, https://doi.org/10.1016/j.jcis.2023.09.047.

[7] X. Lu, P. Yang, Y. Wan, H. Zhang, H. Xu, L. Xiao, R. Li, Y. Li, J. Zhang, M. An, Active site engineering toward atomically dispersed M−N−C catalysts for oxygen reduction reaction, Coord. Chem. Rev. 495 (2023) 215400, https://doi.org/10.1016/j.ccr.2023.215400.

[8] U. Martinez, S. Komini Babu, E.F. Holby, H.T. Chung, X. Yin, P. Zelenay, Progress in the development of Fe-based PGM-free electrocatalysts for the oxygen reduction reaction, Adv. Mater. 31 (2019) 1–20, https://doi.org/10.1002/adma.201806545.

[9] W. Wang, Q. Jia, S. Mukerjee, S. Chen, Recent insights into the oxygen-reduction electrocatalysis of Fe/N/C materials, ACS Catal. 9 (2019) 10126–10141, https://doi.org/10.1021/acscatal.9b02583.

[10] M. Xiao, J. Zhu, L. Ma, Z. Jin, J. Ge, X. Deng, Y. Hou, Q. He, J. Li, Q. Jia, S. Mukerjee, R. Yang, Z. Jiang, D. Su, C. Liu, W. Xing, Microporous framework induced synthesis of single-atom dispersed Fe-N-C acidic ORR catalyst and its in situ reduced Fe-N_4 active site identification revealed by X-ray absorption spectroscopy, ACS Catal. 8 (2018) 2824–2832, https://doi.org/10.1021/acscatal.8b00138.

[11] Y. Han, Y. Wang, R. Xu, W. Chen, L. Zheng, A. Han, Y. Zhu, J. Zhang, H. Zhang, J. Luo, C. Chen, Q. Peng, D. Wang, Y. Li, Electronic structure engineering to boost oxygen reduction activity by controlling the coordination of the central metal, Energy Environ. Sci. 11 (2018) 2348–2352, https://doi.org/10.1039/C8EE01481G.

[12] C.-X. Zhao, B.-Q. Li, J.-N. Liu, Q. Zhang, Intrinsic electrocatalytic activity regulation of M-N-C single-atom catalysts for the oxygen reduction reaction, Angew. Chem. Int. Ed. 60 (2021) 4448–4463, https://doi.org/10.1002/anie.202003917.

[13] C. Shao, L. Wu, Y. Wang, K. Qu, H. Chu, L. Sun, J. Ye, B. Li, X. Wang, Engineering asymmetric Fe coordination centers with hydroxyl adsorption for efficient and durable oxygen reduction catalysis, Appl. Catal. B Environ. 316 (2022) 121607, https://doi.org/10.1016/j.apcatb.2022.121607.

[14] Z. Chen, H. Niu, J. Ding, H. Liu, P.-H. Chen, Y. Lu, Y.-R. Lu, W. Zuo, L. Han, Y. Guo, S.-F. Hung, Y. Zhai, Unraveling the origin of sulfur-doped Fe-N-C single-atom catalyst for enhanced oxygen reduction activity: effect of iron spin-state tuning, Angew. Chem. Int. Ed. 60 (2021) 25404–25410, https://doi.org/10.1002/anie.202110243.

[15] J. Zhang, Y. Zhao, C. Chen, Y.C. Huang, C.L. Dong, C.J. Chen, R.S. Liu, C. Wang, K. Yan, Y. Li, G. Wang, Tuning the coordination environment in single-atom catalysts to achieve highly efficient oxygen reduction reactions, J. Am. Chem. Soc. 141 (2019) 20118–20126, https://doi.org/10.1021/jacs.9b09352.

[16] E. Zhu, C. Sun, C. Shi, J. Yu, X. Yang, M. Xu, Isolated single-atom Fe-N$_4$O$_1$ catalytic site from a pre-oxidation strategy for efficient oxygen reduction reaction, Chem. Eng. J. 463 (2023) 142468, https://doi.org/10.1016/j.cej.2023.142468.

[17] Y. Wang, J. Wu, S. Tang, J. Yang, C. Ye, J. Chen, Y. Lei, D. Wang, Synergistic Fe−Se atom pairs as bifunctional oxygen electrocatalysts boost low-temperature rechargeable Zn–air battery, Angew. Chem. Int. Ed. 62 (2023), https://doi.org/10.1002/anie.202219191.

[18] Y. Zhou, X. Tao, G. Chen, R. Lu, D. Wang, M. Chen, E. Jin, J. Yang, H. Liang, Y. Zhao, X. Feng, A. Narita, K. Müllen, Multilayer stabilization for fabricating high-loading single-atom catalysts, Nat. Commun. 11 (2020) 5892, https://doi.org/10.1038/s41467-020-19599-8.

[19] L. Jiao, R. Zhang, G. Wan, W. Yang, X. Wan, H. Zhou, J. Shui, S. Yu, H. Jiang, Nanocasting SiO$_2$ into metal–organic frameworks imparts dual protection to high-loading Fe single-atom electrocatalysts, Nat. Commun. 11 (2020) 2831, https://doi.org/10.1038/s41467-020-16715-6.

[20] C. Jiao, Z. Xu, J. Shao, Y. Xia, J. Tseng, G. Ren, N. Zhang, P. Liu, C. Liu, G. Li, S. Chen, S. Chen, H. Wang, High-density atomic Fe–N$_4$/C in tubular, biomass-derived, nitrogen-rich porous carbon as air-electrodes for flexible Zn–air batteries, Adv. Funct. Mater. 33 (2023), https://doi.org/10.1002/adfm.202213897.

[21] X. Lu, H. Xu, P. Yang, L. Xiao, Y. Li, J. Ma, R. Li, L. Liu, A. Liu, V. Kondratiev, O. Levin, J. Zhang, M. An, Zinc-assisted MgO template synthesis of porous carbon-supported Fe-N$_x$ sites for efficient oxygen reduction reaction catalysis in Zn-air batteries, Appl. Catal. B Environ. 313 (2022) 121454, https://doi.org/10.1016/j.apcatb.2022.121454.

[22] W. Niu, J. He, B. Gu, M. Liu, Y. Chueh, Opportunities and challenges in precise synthesis of transition metal single-atom supported by 2D materials as catalysts toward oxygen reduction reaction, Adv. Funct. Mater. 31 (2021) 2103558, https://doi.org/10.1002/adfm.202103558.

[23] C.-C. Weng, J.-T. Ren, H.-Y. Wang, X.-W. Lv, Y.-J. Song, Y.-S. Wang, L. Chen, W.-W. Tian, Z.-Y. Yuan, Triple-phase oxygen electrocatalysis of hollow spherical structures for rechargeable Zn-air batteries, Appl. Catal. B Environ. 307 (2022) 121190, https://doi.org/10.1016/j.apcatb.2022.121190.

[24] Z.-F. Huang, J. Song, S. Dou, X. Li, J. Wang, X. Wang, Strategies to break the scaling relation toward enhanced oxygen electrocatalysis, Matter 1 (2019) 1494–1518, https://doi.org/10.1016/j.matt.2019.09.011.

[25] A. Khorshidi, J. Violet, J. Hashemi, A.A. Peterson, How strain can break the scaling relations of catalysis, Nat. Catal. 1 (2018) 263–268, https://doi.org/10.1038/s41929-018-0054-0.

[26] Y. Zhou, R. Lu, X. Tao, Z. Qiu, G. Chen, J. Yang, Y. Zhao, X. Feng, K. Müllen, Boosting oxygen electrocatalytic activity of Fe–N–C catalysts by phosphorus incorporation, J. Am. Chem. Soc. 145 (2023) 3647–3655, https://doi.org/10.1021/jacs.2c12933.

[27] J. Li, K. Fan, H. Jiang, F. Lu, L. Cui, B. Li, Q. Zhang, G.C. Fan, L. Zong, L. Wang, Boosting the oxygen reduction reaction behaviour of atomic Fe-N$_4$ active sites in porous honeycomb-like carbon via P heteroatom doping, J. Mater. Chem. A. 10 (2022) 18147–18155, https://doi.org/10.1039/d2ta04255j.

[28] Y. Pan, X. Ma, M. Wang, X. Yang, S. Liu, H. Chen, Z. Zhuang, Y. Zhang, W. Cheong, C. Zhang, X. Cao, R. Shen, Q. Xu, W. Zhu, Y. Liu, X. Wang, X. Zhang, W. Yan, J. Li, H.M. Chen, C. Chen, Y. Li, Construction of N, P co-doped carbon frames anchored with Fe single atoms and Fe$_2$P nanoparticles as a robust coupling catalyst for electrocatalytic oxygen reduction, Adv. Mater. 34 (2022) 2203621, https://doi.org/10.1002/adma.202203621.

[29] H. Yin, P. Yuan, B.A. Lu, H. Xia, K. Guo, G. Yang, G. Qu, D. Xue, Y. Hu, J. Cheng, S. Mu, J.N. Zhang, Phosphorus-driven electron delocalization on edge-type FeN$_4$ active sites for oxygen reduction in acid medium, ACS Catal. 11 (2021) 12754–12762, https://doi.org/10.1021/acscatal.1c02259.

[30] A. Nairan, C. Liang, S.W. Chiang, Y. Wu, P. Zou, U. Khan, W. Liu, F. Kang, S. Guo, J. Wu, C. Yang, Proton selective adsorption on Pt-Ni nano-thorn array electrodes for superior hydrogen evolution activity, Energy Environ. Sci. 14 (2021) 1594–1601, https://doi.org/10.1039/d1ee00106j.

[31] H. Li, C. Cai, Q. Wang, S. Chen, J. Fu, B. Liu, Q. Hu, K. Hu, H. Li, J. Hu, Q. Liu, S. Chen, M. Liu, High-performance alkaline water splitting by Ni nanoparticle-decorated Mo-Ni microrods: enhanced ion adsorption by the local electric field, Chem. Eng. J. 435 (2022) 134860, https://doi.org/10.1016/j.cej.2022.134860.

[32] P. An, L. Wei, H. Li, B. Yang, K. Liu, J. Fu, H. Li, H. Liu, J. Hu, Y.R. Lu, H. Pan, T. S. Chan, N. Zhang, M. Liu, Enhancing CO$_2$ reduction by suppressing hydrogen evolution with polytetrafluoroethylene protected copper nanoneedles, J. Mater. Chem. A. 8 (2020) 15936–15941, https://doi.org/10.1039/d0ta03645e.

[33] M. Liu, Y. Pang, B. Zhang, P. De Luna, O. Voznyy, J. Xu, X. Zheng, C.T. Dinh, F. Fan, C. Cao, F.P.G. De Arquer, T.S. Safaei, A. Mepham, A. Klinkova, E. Kumacheva, T. Filleter, D. Sinton, S.O. Kelley, E.H. Sargent, Enhanced electrocatalytic CO$_2$ reduction via field-induced reagent concentration, Nature 537 (2016) 382–386, https://doi.org/10.1038/nature19060.

[34] J.-X. Gao, H. Zhang, X.-D. Yi, P.-P. Xu, C.-L. Tang, H.-L. Wan, K.-R. Tsai, T. Ikariya, New chiral catalysts for reduction of ketones, Chirality 12 (2000) 383–388, https://doi.org/10.1002/(SICI)1520-636X(2000)12:5/6<383::AID-CHIR15>3.0.CO;2-C.

[35] D. Zhang, E.-Z. Zhu, Z.-W. Lin, Z.-B. Wei, Y.-Y. Li, J.-X. Gao, Enantioselective hydrogenation of ketones catalyzed by chiral cobalt complexes containing PNNP ligand, Asian J. Org. Chem. 5 (2016) 1323–1326, https://doi.org/10.1002/ajoc.201600358.

[36] X. Cheng, J. Yang, W. Yan, Y. Han, X. Qu, S. Yin, C. Chen, R. Ji, Y. Li, G. Li, G. Li, Y. Jiang, S. Sun, Nano-geometric deformation and synergistic Co nanoparticles—Co-N$_4$ composite sites for proton exchange membrane fuel cells, Energy Environ. Sci. 14 (2021) 5958–5967, https://doi.org/10.1039/D1EE01715B.

[37] S.J. Clark, M.D. Segall, C.J. Pickard, P.J. Hasnip, M.I.J. Probert, K. Refson, M. C. Payne, First principles methods using CASTEP, Z. Für Krist. - Cryst. Mater. 220 (2005) 567–570, https://doi.org/10.1524/zkri.220.5.567.65075.

[38] D. Yuan, Y. Dou, C.T. He, L. Yu, L. Xu, D. Adekoya, Q. Xia, J. Ma, S.X. Dou, S. Zhang, Sulfur doping optimized intermediate energetics of FeCoOOH for enhanced oxygen evolution catalytic activity, Cell Rep. Phys. Sci. 2 (2021), https://doi.org/10.1016/j.xcrp.2021.100331.

[39] T. Zheng, J. Xiong, B. Zhu, X. Shi, Y.J. Cheng, H. Zhao, Y. Xia, From −20 °C to 150 °C: a lithium secondary battery with a wide temperature window obtainedviamanipulated competitive decomposition in electrolyte solution, J. Mater. Chem. A. 9 (2021) 9307–9318, https://doi.org/10.1039/d1ta00895a.

[40] X.Q. Zhang, X. Chen, X.B. Cheng, B.Q. Li, X. Shen, C. Yan, J.Q. Huang, Q. Zhang, Highly stable lithium metal batteries enabled by regulating the solvation of lithium ions in nonaqueous electrolytes, Angew. Chem. - Int. Ed. 57 (2018) 5301–5305, https://doi.org/10.1002/anie.201801513.

[41] T. Zheng, B. Zhu, J. Xiong, T. Xu, C. Zhu, C. Liao, S. Yin, G. Pan, Y. Liang, X. Shi, H. Zhao, R. Berger, Y.-J. Cheng, Y. Xia, P. Müller-Buschbaum, When audience takes stage: pseudo-localized-high-concentration electrolyte with lithium nitrate as the only salt enables lithium metal batteries with excellent temperature and cathode adaptability, Energy Storage Mater. 59 (2023) 102782, https://doi.org/10.1016/j.ensm.2023.102782.

[42] K. Wang, H. Yang, Q. Wang, J. Yu, Y. He, Y. Wang, S. Song, Y. Wang, Electronic enhancement engineering by atomic Fe–N$_4$ Sites for highly-efficient PEMFCs: tailored electric-thermal field on Pt surface, Adv. Energy Mater. 13 (2023) 1–9, https://doi.org/10.1002/aenm.202204371.

[43] Y. Yin, K. Zhai, B. Zhang, S. Zhai, Electrical resistivity of iron phosphides at high-pressure and high-temperature conditions with implications for lunar core's thermal conductivity, J. Geophys. Res. Solid Earth 124 (2019) 5544–5556, https://doi.org/10.1029/2018JB017157.

[44] F. Calle-Vallejo, J.I. Martínez, J. Rossmeisl, Density functional studies of functionalized graphitic materials with late transition metals for oxygen reduction reactions, Phys. Chem. Chem. Phys. 13 (2011) 15639, https://doi.org/10.1039/c1cp21228a.

[45] J.K. Nørskov, J. Rossmeisl, A. Logadottir, L. Lindqvist, J.R. Kitchin, T. Bligaard, H. Jónsson, Origin of the overpotential for oxygen reduction at a fuel-cell cathode, J. Phys. Chem. B. 108 (2004) 17886–17892, https://doi.org/10.1021/jp047349j.

[46] J. Rossmeisl, Z.-W. Qu, H. Zhu, G.-J. Kroes, J.K. Nørskov, Electrolysis of water on oxide surfaces, J. Electroanal. Chem. 607 (2007) 83–89, https://doi.org/10.1016/j.jelechem.2006.11.008.

[47] Z.-Y. Wu, F.-Y. Chen, B. Li, S.-W. Yu, Y.Z. Finfrock, D.M. Meira, Q.-Q. Yan, P. Zhu, M.-X. Chen, T.-W. Song, Z. Yin, H.-W. Liang, S. Zhang, G. Wang, H. Wang, Non-iridium-based electrocatalyst for durable acidic oxygen evolution reaction in proton exchange membrane water electrolysis, Nat. Mater. 22 (2023) 100–108, https://doi.org/10.1038/s41563-022-01380-5.

[48] D. Chen, R. Yu, R. Lu, Z. Pu, P. Wang, J. Zhu, P. Ji, D. Wu, J. Wu, Y. Zhao, Z. Kou, J. Yu, S. Mu, Tunable Ru-Ru$_2$P heterostructures with charge redistribution for efficient pH-universal hydrogen evolution, InfoMat 4 (2022), https://doi.org/10.1002/inf2.12287.

[49] S. Yu, W. Shen, Y. Li, Z. Dong, Y. Xu, Q. Li, J. Zhang, J. Gao, Iron-catalyzed highly enantioselective reduction of aromatic ketones with chiral P$_2$N$_4$-type macrocycles, Adv. Synth. Catal. 354 (2012) 818–822, https://doi.org/10.1002/adsc.201100733.

[50] G.Y. Zhang, S.H. Ruan, Y.Y. Li, J.X. Gao, Manganese catalyzed asymmetric transfer hydrogenation of ketones, Chin. Chem. Lett. 32 (2021) 1415–1418, https://doi.org/10.1016/j.cclet.2020.10.023.

[51] J. Zhang, X. Yang, H. Zhou, Y. Li, Z. Dong, J. Gao, Oxidative kinetic resolution of racemic secondary alcohols in water with chiral PNNP/Ir catalyst, Green. Chem. 14 (2012) 1289–1292, https://doi.org/10.1039/c2gc00028h.

[52] S. Chen, L. Zhao, J. Ma, Y. Wang, L. Dai, J. Zhang, Edge-doping modulation of N, P-codoped porous carbon spheres for high-performance rechargeable Zn-air batteries, Nano Energy 60 (2019) 536–544, https://doi.org/10.1016/j.nanoen.2019.03.084.

[53] H. Luo, T. Shan, J. Zhou, L. Huang, L. Chen, R. Sa, Y. Yamauchi, J. You, Y. Asakura, Z. Yuan, H. Xiao, Controlled synthesis of hollow carbon ring incorporated g-C$_3$N$_4$ tubes for boosting photocatalytic H$_2$O$_2$ production, Appl. Catal. B Environ. 337 (2023) 122933, https://doi.org/10.1016/j.apcatb.2023.122933.

[54] M.S. Nasir, G. Yang, I. Ayub, S. Wang, L. Wang, X. Wang, W. Yan, S. Peng, S. Ramakrishna, Recent development in graphitic carbon nitride based photocatalysis for hydrogen generation, Appl. Catal. B Environ. 257 (2019) 117855, https://doi.org/10.1016/j.apcatb.2019.117855.

[55] J. Zhang, Y. Zhao, C. Chen, Y.-C. Huang, C.-L. Dong, C.-J. Chen, R.-S. Liu, C. Wang, K. Yan, Y. Li, G. Wang, Tuning the coordination environment in single-atom catalysts to achieve highly efficient oxygen reduction reactions, J. Am. Chem. Soc. 141 (2019) 20118–20126, https://doi.org/10.1021/jacs.9b09352.

[56] M. Xiao, J. Zhu, L. Ma, Z. Jin, J. Ge, X. Deng, Y. Hou, Q. He, J. Li, Q. Jia, S. Mukerjee, R. Yang, Z. Jiang, D. Su, C. Liu, W. Xing, Microporous framework induced synthesis of single-atom dispersed Fe-N-C acidic ORR catalyst and its in situ reduced Fe-N$_4$ active site identification revealed by X-ray absorption spectroscopy, ACS Catal. 8 (2018) 2824–2832, https://doi.org/10.1021/acscatal.8b00138.

[57] R. Kothandaraman, V. Nallathambi, K. Artyushkova, S.C. Barton, Non-precious oxygen reduction catalysts prepared by high-pressure pyrolysis for low-temperature fuel cells, Appl. Catal. B Environ. 92 (2009) 209–216, https://doi.org/10.1016/j.apcatb.2009.07.005.

[58] L. Jiao, G. Wan, R. Zhang, H. Zhou, S. Yu, H. Jiang, From metal–organic frameworks to single-atom Fe implanted N-doped porous carbons: efficient oxygen

reduction in both alkaline and acidic media, Angew. Chem. Int. Ed. 57 (2018) 8525–8529, https://doi.org/10.1002/anie.201803262.

[59] S. Ji, B. Jiang, H. Hao, Y. Chen, J. Dong, Y. Mao, Z. Zhang, R. Gao, W. Chen, R. Zhang, Q. Liang, H. Li, S. Liu, Y. Wang, Q. Zhang, L. Gu, D. Duan, M. Liang, D. Wang, Matching the kinetics of natural enzymes with a single-atom iron nanozyme, Nat. Catal. 4 (2021), https://doi.org/10.1038/s41929-021-00609-x.

[60] Y. Li, B. Chen, X. Duan, S. Chen, D. Liu, K. Zang, R. Si, F. Lou, X. Wang, M. Rønning, L. Song, J. Luo, D. Chen, Atomically dispersed Fe-N-P-C complex electrocatalysts for superior oxygen reduction, Appl. Catal. B Environ. 249 (2019) 306–315, https://doi.org/10.1016/j.apcatb.2019.03.016.

[61] S. Hou, A. Zhang, Q. Zhou, Y. Wen, S. Zhang, L. Su, X. Huang, T. Wang, K. Rui, C. Wang, H. Liu, Z. Lu, P. He, Designing heterostructured FeP-CoP for oxygen evolution reaction: interface engineering to enhance electrocatalytic performance, Nano Res 16 (2023) 6601–6607, https://doi.org/10.1007/s12274-023-5390-y.

[62] H. Zheng, F. Ma, H. Yang, X. Wu, R. Wang, D. Jia, Z. Wang, N. Lu, F. Ran, S. Peng, Mn, N co-doped Co nanoparticles/porous carbon as air cathode for highly efficient rechargeable Zn-air batteries, Nano Res. 15 (2022) 1942–1948, https://doi.org/10.1007/s12274-021-3837-6.